



Analysis of Magnetohydrodynamic Perturbations in the Radial-field Solar Wind from Parker Solar Probe Observations

S. Q. Zhao, Huirong Yan, Terry Z. Liu, Mingzhe Liu, Mijie Shi

► To cite this version:

S. Q. Zhao, Huirong Yan, Terry Z. Liu, Mingzhe Liu, Mijie Shi. Analysis of Magnetohydrodynamic Perturbations in the Radial-field Solar Wind from Parker Solar Probe Observations. The Astrophysical Journal, 2021, 923, 10.3847/1538-4357/ac2ffe . insu-03713735

HAL Id: insu-03713735

<https://insu.hal.science/insu-03713735>

Submitted on 5 Jul 2022

HAL is a multi-disciplinary open access archive for the deposit and dissemination of scientific research documents, whether they are published or not. The documents may come from teaching and research institutions in France or abroad, or from public or private research centers.

L'archive ouverte pluridisciplinaire **HAL**, est destinée au dépôt et à la diffusion de documents scientifiques de niveau recherche, publiés ou non, émanant des établissements d'enseignement et de recherche français ou étrangers, des laboratoires publics ou privés.



Distributed under a Creative Commons Attribution| 4.0 International License



Analysis of Magnetohydrodynamic Perturbations in the Radial-field Solar Wind from Parker Solar Probe Observations

S. Q. Zhao^{1,2} , Huirong Yan^{1,2} , Terry Z. Liu³ , Mingzhe Liu⁴ , and Mijie Shi⁵

¹ Deutsches Elektronen Synchrotron (DESY), Platanenallee 6, D-15738, Zeuthen, Germany; huirong.yan@desy.de

² Institut für Physik und Astronomie, Universität Potsdam, D-14476, Potsdam, Germany

³ Department of Earth, Planetary, and Space Sciences, University of California, Los Angeles, California, USA

⁴ LESIA, Observatoire de Paris, Université PSL, CNRS, Sorbonne Université, Université de Paris, place Jules Janssen, 92195, Meudon, France

⁵ Centre for mathematical Plasma Astrophysics, Department of Mathematics, KU Leuven, B-3001 Leuven, Belgium

Received 2021 June 2; revised 2021 October 13; accepted 2021 October 13; published 2021 December 28

Abstract

We report analysis of sub-Alfvénic magnetohydrodynamic (MHD) perturbations in the low- β radial-field solar wind employing the Parker Solar Probe spacecraft data from 2018 October 31 to November 12. We calculate wavevectors using the singular value decomposition method and separate MHD perturbations into three eigenmodes (Alfvén, fast, and slow modes) to explore the properties of sub-Alfvénic perturbations and the role of compressible perturbations in solar wind heating. The MHD perturbations show a high degree of Alfvénicity in the radial-field solar wind, with the energy fraction of Alfvén modes dominating ($\sim 45\%$ – 83%) over those of fast modes ($\sim 16\%$ – 43%) and slow modes ($\sim 1\%$ – 19%). We present a detailed analysis of a representative event on 2018 November 10. Observations show that fast modes dominate magnetic compressibility, whereas slow modes dominate density compressibility. The energy damping rate of compressible modes is comparable to the heating rate, suggesting the collisionless damping of compressible modes could be significant for solar wind heating. These results are valuable for further studies of the imbalanced turbulence near the Sun and possible heating effects of compressible modes at MHD scales in low- β plasma.

Unified Astronomy Thesaurus concepts: Solar wind (1534); Interplanetary turbulence (830); Magnetohydrodynamics (1964); Space plasmas (1544); Stellar winds (1636)

1. Introduction

Plasma turbulence appears ubiquitous and plays a crucial role in various astrophysical processes, such as solar wind heating and acceleration (e.g., Bandyopadhyay et al. 2020), scattering of cosmic rays (e.g., Yan 2015), turbulent heating in galaxy clusters (e.g., Zhuravleva et al. 2014), and star formation (e.g., Federrath 2018). Turbulence is typically characterized by a broadband spectrum of perturbations, energy transmission spanning a vast range of temporal and spatial scales, highly chaotic but self-similar motions within the inertial range. The solar wind, a plasma flow originating from the Sun and continuously blowing into the interplanetary space, provides an excellent laboratory for studying plasma turbulence at magnetohydrodynamic (MHD) and sub-ion-kinetic scales (e.g., Dobrowolny et al. 1980; Verscharen et al. 2019). MHD perturbations can be decomposed into three eigenmodes: Alfvén, fast, and slow modes (e.g., Glassmeier et al. 1995; Cho & Lazarian 2003). Using the term *mode* in this study, we refer to the carriers of turbulent perturbations in wave turbulence rather than classical linear waves (e.g., Cho & Lazarian 2003; Verscharen et al. 2019). The mode composition affects almost all turbulence dynamics and the mechanisms of solar wind heating (e.g., Suzuki et al. 2006; Cranmer & van Ballegooijen 2012; Makwana & Yan 2020). Clarifying the mode composition and the properties of each mode can help us further understand astrophysical mysteries, e.g., corona

heating; transport of particles (Chandran 2005; Yan & Lazarian 2008).

The MHD mode composition has been extensively investigated through simulations and satellite observations (e.g., Cho & Lazarian 2003; Chaston et al. 2020; Makwana & Yan 2020; Zhu et al. 2020). Simulations of MHD turbulence found that different modes cascade differently. The cascade of Alfvén and slow modes is anisotropic, mainly in the direction perpendicular to the local background magnetic field, whereas fast modes tend to show isotropic cascade (e.g., Cho & Lazarian 2003; Makwana & Yan 2020). Furthermore, satellite observations with a mode composition diagnostic (Glassmeier et al. 1995) show that anti-sunward propagating Alfvén modes dominate mode composition, and energy fraction enhancements of compressible modes are associated with the background magnetic field variations (e.g., Chaston et al. 2020; Zhu et al. 2020).

The compressible modes affect the compressibility of solar wind turbulence and thus influence other turbulence properties (e.g., Chen et al. 2019). Magnetic compressibility, defined as $C_{BB} = \left(\frac{\delta|\mathbf{B}|}{|\delta\mathbf{B}|} \right)^2$, is observed to increase with the heliocentric distance (e.g., Bavassano et al. 1982; Chen et al. 2019; Andrés et al. 2021). Howes et al. (2012) indicated that compressible components of solar wind turbulence at the inertial range mainly result from the kinetic slow mode. Additionally, Chen et al. (2019) suggested that magnetic compressibility depends on plasma β and slow-mode perturbations with the assumption of $\delta\mathbf{B}_\perp$ from Alfvén modes and $\delta|\mathbf{B}| \approx \delta B_\parallel$ from slow modes. Then a straightforward but critical question is whether the assumption of the magnetic compressible component (δB_\parallel) from slow modes is still valid in quiet radial-field solar wind



Original content from this work may be used under the terms of the [Creative Commons Attribution 4.0 licence](https://creativecommons.org/licenses/by/4.0/). Any further distribution of this work must maintain attribution to the author(s) and the title of the work, journal citation and DOI.

turbulence (e.g., Bale et al. 2019). The normalized radial magnetic field is required to satisfy $\frac{|B_R|}{|B|} > 0.8$ in this study, where B_R represents the magnetic field along the direction of the Sun to the spacecraft in radial tangential normal (RTN) coordinates. To investigate the possible origins of magnetic and density compressibility, we separate the MHD perturbations into three eigenmodes using the mode decomposition method (Cho & Lazarian 2003) to explore the role of each mode in kinetic, magnetic, and density power spectra.

The collisionless damping of plasma waves plays a critical role in plasma heating (e.g., Suzuki et al. 2006; Zhuravleva et al. 2014). In the MHD regime, collisionless damping of compressible modes is widely considered a possible heating mechanism (e.g., Porter et al. 1994; Kumar et al. 2006; Petrosian et al. 2006; Spanier & Schlickeiser 2005). Therefore, another critical question, which is not well understood, is about the possible heating effects of each mode. Alfvén modes are non-compressive and can only be damped ohmically or by shear viscosity. Thus, Alfvén modes are weakly damped in a plasma with Maxwellian distributions, making limited contributions to plasma heating in the linear regime. By contrast, compressible magnetosonic modes (fast and slow modes) are prone to intense collisionless damping owing to wave-particle interactions, providing an efficient energy conversion between waves and plasmas (e.g., Ginzburg 1961; Barnes 1967). The compressible MHD perturbations are typically interpreted as a mixture of fast magnetosonic waves and pressure-balanced structures (PBSs). The PBS is characterized by an anticorrelation of thermal and magnetic pressure, similar to that of slow modes (e.g., Howes et al. 2012; Bruno & Carbone 2013). Therefore, mode decomposition provides a valuable tool for quantitatively analyzing the possible role of each mode in plasma heating.

The Parker Solar Probe (PSP) mission is well situated to investigate the properties of the near-Sun turbulence with the nearest heliocentric distance of ~ 0.17 au during its first encounter. This study applies the mode decomposition method (Cho & Lazarian 2003) to in situ spacecraft observations to study sub-Alfvénic MHD perturbations in the solar wind for the first time. This new mode decomposition method makes it possible to quantitatively analyze the role of each MHD mode in kinetic, magnetic, and density power spectra and the contributions of each mode on magnetic and density compressibility. Moreover, we determine the collisionless damping of each mode to reveal the role of compressible modes in solar wind heating. The outline of this paper is as follows. Section 2 presents data sets, search criteria, and analysis methods used in this study. Section 3 offers a representative case to analyze the mode composition of the MHD perturbations and the possible role compressible modes play in solar wind heating. In Sections 4 and 5, we discuss and conclude our results.

2. Data and Mode Decomposition

2.1. Data

We utilize data measured by NASA’s PSP mission (Fox et al. 2016) during its first perihelion. We analyze magnetic field data from the fluxgate magnetometer (MAG; Bale et al. 2016), proton parameters with a ~ 0.874 s resolution from the Solar Probe Cup (SPC; Kasper et al. 2016), and electron parameters with a 7 s resolution deduced from the simplified quasi-thermal noise (QTN) method with observations from the

Radio Frequency Spectrometer (FIELDS; Moncuquet et al. 2020). The electric field data at MHD scales are calculated by $\mathbf{E} = -\mathbf{V}_p \times \mathbf{B}$, where \mathbf{V}_p is the proton bulk velocity and \mathbf{B} is the magnetic field. The observed parameters consist of the ensemble average background field and a fluctuating field, i.e., $\mathbf{B} = \mathbf{B}_0 + \mathbf{b}$, $\mathbf{V}_p = \mathbf{V}_0 + \mathbf{v}$, $\mathbf{E} = \mathbf{E}_0 + \mathbf{e}$, and $N_p = N_0 + n$. The magnetic field perturbation \mathbf{b} , presented in Alfvén speed units, is normalized by $\sqrt{\mu_0 \rho_0} = \sqrt{\mu_0 m_p N_0}$, where μ_0 is the vacuum permeability, ρ_0 is the mean proton mass density, and m_p is the proton mass. The ensemble average in this study is represented by a time average over each 250 s interval.

2.2. Data Selection Criteria

The first PSP encounter spans from 2018 October 31 to November 12, covering the heliocentric distance between 0.166 and 0.277 au. We search for events that satisfy four criteria: (1) sub-Alfvénic ($v \ll V_A$ and $b \ll B_0$) perturbations, where V_A is the Alfvén speed. Under such a condition, the nonlinear terms (v^2 , b^2) are much less than the linear terms ($V_A \cdot v$, $B_0 \cdot b$), and thus perturbations can roughly be considered as a pure superposition of three MHD modes. (2) Large normalized radial magnetic field ($\frac{|B_R|}{|B|} > 0.8$). In the radial-field solar wind, the small (quasi-parallel/quasi-antiparallel) flow-to-field angles θ_{BV} indicate wavevectors along the field larger than that across it, $k_{\parallel} \gg k_{\perp} \sim 0$. Thus, these low-amplitude and field-aligned perturbations exhibit more wave-like characteristics than turbulence (e.g., Bale et al. 2019). (3) High electromagnetic planarity $> +0.8$ (Santolík et al. 2003) means the validity of planarity assumption, guaranteeing that small perturbations can be written as Fourier components ($e^{i(\mathbf{k} \cdot \mathbf{x} - \omega t)}$) in the linearization of MHD equations. It is the foundation both of the singular value decomposition (SVD) method and the mode decomposition method. (4) The event duration should be longer than 20 minutes to ensure the measurements of low-frequency signals. During the first PSP encounter, a total of 15 events are identified and listed in Table 1. The representative case analyzed in Section 3 corresponds to event #15 in the table and the shaded area in Figure 1.

2.3. The Measurements of the Dispersion Relations

To measure the observed dispersion relations, we first determine wavevectors \mathbf{k} using the SVD method of Santolík et al. (2003). The SVD method holds under the assumption of a single plane wave. This technique provides a mathematical approach to obtain the frequency-time spectrograms of \mathbf{k} through solving the linearized Faraday’s law: $\mathbf{k} \times \mathbf{E}(\omega_{sc}, t) = \omega_{sc} \mathbf{B}(\omega_{sc}, t)$, where complex matrices of electric and magnetic field ($\mathbf{E}(\omega_{sc}, t)$ and $\mathbf{B}(\omega_{sc}, t)$) are obtained through the Morlet-wavelet transform (Grinsted et al. 2004) and $\omega_{sc} = 2\pi f_{sc}$ is the observed frequency in the spacecraft frame. Then, according to the Doppler shift, the observed frequency in the plasma flow frame can be obtained by $\omega_{pf} = \omega_{sc} - \langle \mathbf{k} \rangle \cdot \langle \mathbf{V}_p \rangle$, where $\langle \rangle$ represents the time average. The observed dispersion relations will be compared with the theoretical ones obtained from the mode decomposition method, as detailed below.

2.4. Mode Decomposition Methods

We utilize Cho & Lazarian’s (2003) method to decompose the MHD perturbations into three eigenmodes: Alfvén, slow, and fast modes. The three modes share the same wavevector. We first use \mathbf{k} and \mathbf{B}_0 to build a new coordinate:

Table 1
List of Identified Radial-field Solar Wind Turbulence from 2018 October 31 to November 12

No.	Start Time (UT)	End Time (UT)	Scale (minutes)	$\langle\beta\rangle$	$\langle a \rangle$ (km s ⁻¹)	$\langle V_A \rangle$ (km s ⁻¹)	θ_{kB0} (deg)	P_{KEA}	P_{MEA}	P_{KEf}	P_{MEf}	P_{KEs}	P_{MEs}
1	2018-11-02/16:14:00	2018-11-02/17:22:00	68	0.19	41	102	167	29%	28%	20%	20%	3%	$\ll 1\%$
2	2018-11-03/04:13:00	2018-11-03/05:04:00	51	0.21	41	98	169	35%	34%	13%	13%	5%	$\ll 1\%$
3	2018-11-04/19:13:00	2018-11-04/19:58:00	45	0.28	50	105	170	27%	27%	21%	21%	4%	$\ll 1\%$
4	2018-11-05/00:22:00	2018-11-05/01:23:00	61	0.26	50	107	170	29%	28%	20%	20%	3%	$\ll 1\%$
5	2018-11-05/15:58:00	2018-11-05/16:31:00	33	0.28	50	103	169	27%	26%	22%	21%	4%	$\ll 1\%$
6	2018-11-05/20:05:00	2018-11-05/21:03:00	58	0.16	47	128	161	23%	22%	19%	19%	16%	$\ll 1\%$
7	2018-11-05/21:35:00	2018-11-05/22:58:00	83	0.18	45	118	169	28%	27%	21%	20%	4%	$\ll 1\%$
8	2018-11-07/04:57:00	2018-11-07/05:22:00	25	0.17	43	115	170	30%	28%	20%	19%	3%	$\ll 1\%$
9	2018-11-07/09:20:00	2018-11-07/10:13:00	53	0.17	70	185	158	29%	28%	17%	16%	9%	$\ll 1\%$
10	2018-11-08/07:03:00	2018-11-08/07:59:00	56	0.16	52	142	169	36%	34%	14%	14%	2%	$\ll 1\%$
11	2018-11-08/16:03:00	2018-11-08/16:39:00	36	0.10	48	165	160	42%	41%	8%	8%	1%	$\ll 1\%$
12	2018-11-10/00:31:00	2018-11-10/01:20:00	49	0.42	81	136	159	26%	24%	21%	19%	9%	1%
13	2018-11-10/12:00:00	2018-11-10/12:38:00	38	0.18	55	143	165	25%	25%	18%	18%	14%	$\ll 1\%$
14	2018-11-10/15:40:00	2018-11-10/16:35:00	55	0.12	45	143	157	24%	24%	17%	16%	19%	$\ll 1\%$
15	2018-11-10/19:30:30	2018-11-10/20:14:30	44	0.18	47	119	163	31%	31%	17%	16%	5%	$\ll 1\%$

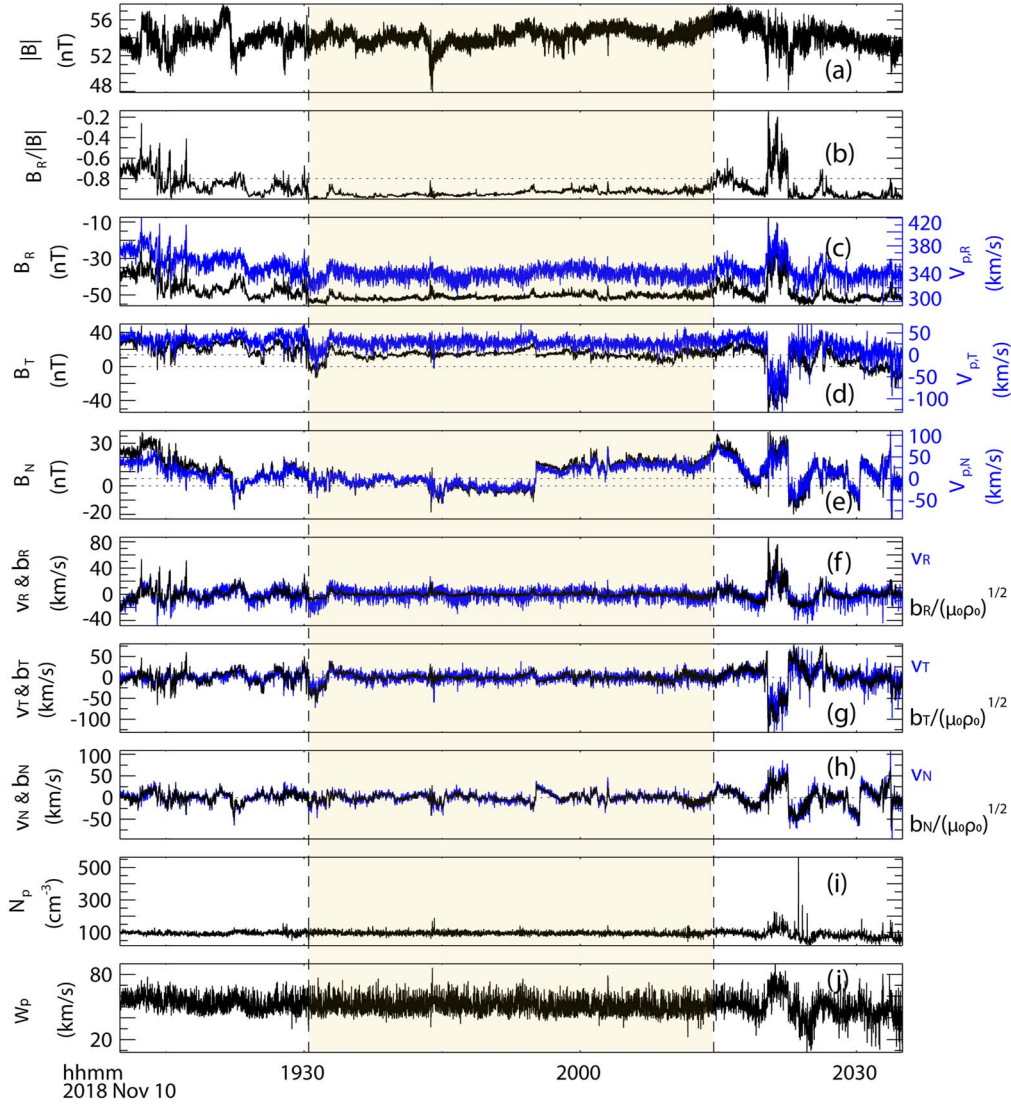


Figure 1. PSP observations of a representative case on 2018 November 10 in RTN coordinates within the yellow shaded region. (a) magnetic field magnitude $|B|$; (b) normalized radial magnetic field $B_R/|B|$; (c) radial magnetic field (B_R , black) and proton bulk velocity ($V_{p,R}$, blue); (d) the tangential components of magnetic field (B_T , black) and proton bulk velocity ($V_{p,T}$, blue); (e) the normal components of magnetic field (B_N , black) and proton bulk velocity ($V_{p,N}$, blue); (f), (h) high correlations between the magnetic field perturbation b and proton bulk velocity v , where b is shown in Alfvén speed units. (i) proton density; (j) proton thermal velocity. RTN: radial tangential normal coordinates.

$\xi = \xi_{\perp} \hat{k}_{\perp} + \xi_{\parallel} \hat{k}_{\parallel} + \xi_{\varphi} \hat{\varphi}$ in wavevector space, where displacement vectors ξ are defined through $\frac{\partial \xi}{\partial t} = \mathbf{v}_k$, and \mathbf{v}_k is velocity perturbation in wavevector space. \hat{k}_{\perp} ($\perp \mathbf{B}_0$), \hat{k}_{\parallel} ($\parallel \mathbf{B}_0$), and $\hat{\varphi} = \hat{k}_{\perp} \times \hat{k}_{\parallel}$ are unit vectors along the orientations of coordinate axes. The velocity perturbations do not comply with one single mode, i.e., shear Alfvén mode.

The time series of velocity perturbation is transformed into frequency space by fast Fourier transform (FFT). We transform velocity perturbation (\mathbf{v}_f) in the frequency domain into \mathbf{v}_k using the relationship between k and f determined by the SVD method, which connects temporal and spatial space. Because the velocity perturbation of each mode is along respective displacement vectors at each wavevector scale, \mathbf{v}_k is projected onto the corresponding ξ (i.e., $\xi_{\text{Alfvén}}$, ξ_{slow} , and ξ_{fast} , see Figure 2(a)). The velocity perturbation, magnetic field, and density of each mode are given by

$$\mathbf{v}_k = \mathbf{v}_{k,\text{Alfvén}} + \mathbf{v}_{k,\text{slow}} + \mathbf{v}_{k,\text{fast}}, \quad (1)$$

$$\begin{aligned} b_{k,\text{Alfvén}} &= B_0 \frac{v_{k,\text{Alfvén}}}{V_A}; \quad b_{k,\text{slow}} = B_0 \frac{v_{k,\text{slow}}}{c_{\text{slow}}} |\hat{\mathbf{B}}_0 \times \hat{\xi}_{\text{slow}}|; \\ b_{k,\text{fast}} &= B_0 \frac{v_{k,\text{fast}}}{c_{\text{fast}}} |\hat{\mathbf{B}}_0 \times \hat{\xi}_{\text{fast}}|, \\ N_k &= N_{k,\text{slow}} + N_{k,\text{fast}} = N_0 \frac{v_{k,\text{slow}}}{c_{\text{slow}}} \hat{k} \cdot \hat{\xi}_{\text{slow}} + N_0 \frac{v_{k,\text{fast}}}{c_{\text{fast}}} \hat{k} \cdot \hat{\xi}_{\text{fast}}. \end{aligned} \quad (2)$$

The displacement vectors ξ are given by

$$\xi_{\text{Alfvén}} = \hat{k}_{\perp} \times \hat{k}_{\parallel}, \quad (4)$$

$$\xi_{\text{slow}} \propto (-1 + \alpha - \sqrt{D}) k_{\parallel} \hat{k}_{\parallel} + (1 + \alpha - \sqrt{D}) k_{\perp} \hat{k}_{\perp}, \quad (5)$$

$$\xi_{\text{fast}} \propto (-1 + \alpha + \sqrt{D}) k_{\parallel} \hat{k}_{\parallel} + (1 + \alpha + \sqrt{D}) k_{\perp} \hat{k}_{\perp}. \quad (6)$$

The subscript k represents parameters in wavevector space, and “ \wedge ” represents corresponding unit vectors. In low- β regime, phase speeds of fast and slow modes (c_{fast} and c_{slow}) are equal

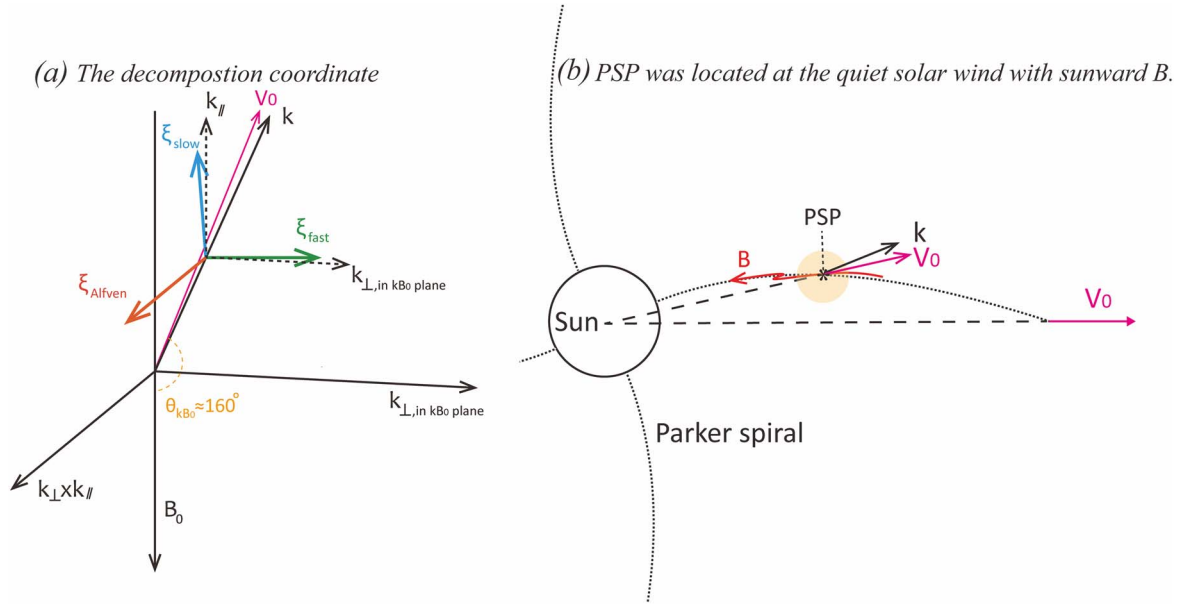


Figure 2. Schematic illustrations of (a) the vectors in the decomposition coordinate at $\theta_{kB_0} \sim 160^\circ$. The displacement vectors ξ : $\xi_{\text{Alfvén}}$ (red), ξ_{fast} (green), and ξ_{slow} (blue). $\xi_{\text{Alfvén}}$ is perpendicular to the kB_0 plane. ξ_{fast} and ξ_{slow} are in the kB_0 plane. The angle between \mathbf{V}_0 and \mathbf{k} is $\sim 2^\circ$ in the kB_0 plane in this event. (b) The relative position between the Sun and PSP.

to V_A (Alfvén speed) and $a \cos \theta_{kB_0}$ (a represents sound speed), respectively. The parameter $D = (1 + \alpha)^2 - 4\alpha \cos \theta_{kB_0}$, where $\alpha = \frac{a^2}{V_A^2}$, and θ_{kB_0} is the wave propagation angle between wavevectors and the background magnetic field.

3. Observations and Results

3.1. Overview of a Representative Case

Figure 1 shows PSP observations of a representative case of sub-Alfvénic perturbations in low- β ($\beta \sim 0.18$) plasma at a heliocentric distance of around 0.229 au on 2018 November 10. The magnetic field and plasma data are shown in RTN coordinates. Figure 1(a) shows that the magnetic field magnitude $|\mathbf{B}|$ is almost constant, indicating weak magnetic compressibility. Figure 1(b) shows that the normalized radial-field magnetic field ($\frac{B_R}{|\mathbf{B}|}$) is less than -0.8 within the yellow shaded region, suggesting that the spacecraft is located at a quiet radial-field solar wind. The corresponding spacecraft relative position is sketched in Figure 2(b), where the open field lines are emerging from the negative-polarity equatorial coronal hole ($B_R < 0$ in Figure 1(c)) during the first PSP encounter (e.g., Bale et al. 2019). In this study, we only focus on the intervals of the sub-Alfvénic non-switchback perturbations. In Figures 1(f)–(h), the magnetic field perturbation ($\mathbf{b} = \mathbf{B} - \langle \mathbf{B} \rangle$) and proton velocity perturbation ($\mathbf{v} = \mathbf{V}_p - \langle \mathbf{V}_p \rangle$) present significantly Alfvénic correlations, where \mathbf{b} is shown in Alfvén speed units. During this time interval, $\mathbf{v} \ll \mathbf{V}_A$ (sub-Alfvénic) and $\mathbf{b} \ll \mathbf{B}_0$. Therefore, the perturbations can be considered as a pure superposition of the three MHD modes. Figure 1(i) shows the proton density with low perturbations. The proton compressibility C_p , defined as $C_p = \frac{\langle n^2 \rangle}{N_0^2} \frac{B_0^2}{\langle \mathbf{b} \cdot \mathbf{b} \rangle}$, is around 0.06, indicating a low level of density compressibility. Figure 1(j) shows proton thermal velocity with small variations.

Figures 3(a)–(c) illustrates spacecraft-frame frequency-time spectrograms of wavevectors in the field-aligned coordinates determined by the average magnetic field (\mathbf{B}_0) and velocity

(\mathbf{V}_0) during 19:30:30–20:14:30 UT (marked by the yellow shaded region in Figure 1), where basis vectors $\mathbf{e}_{\perp 1}$, $\mathbf{e}_{\perp 2}$, and \mathbf{e}_{\parallel} are in the $(\mathbf{v}_0 \times \mathbf{b}_0) \times \mathbf{b}_0$, $\mathbf{v}_0 \times \mathbf{b}_0$, and \mathbf{b}_0 directions, respectively (\mathbf{v}_0 and \mathbf{b}_0 are unit vectors of \mathbf{V}_0 and \mathbf{B}_0). The wavevectors and frequencies are normalized by average proton gyro-radius and gyrofrequency (ρ_{ci} and ω_{ci}), respectively. Figure 3(a)–(c) show spectrograms of absolute values of wavevectors in $\mathbf{e}_{\perp 1}$, $\mathbf{e}_{\perp 2}$, and \mathbf{e}_{\parallel} direction, respectively. We can see that $k_{\parallel} \gg k_{\perp}$, indicating wavevectors along the magnetic field larger than that across it. Moreover, wavevectors are roughly constant in time in the low-frequency range. In Figure 3(d), the high electromagnetic planarity (F_{EB} approaching to 1) indicates the presence of a single plane wave, guaranteeing the validity of the SVD method and mode decomposition method (Cho & Lazarian 2003; Santolík et al. 2003).

3.2. The Role of Each Mode in Kinetic, Magnetic, and Density Power

To facilitate comparison with direct observations, Figure 4 shows the decomposition results in the spacecraft frame during 19:30:30–20:14:30 UT. To reduce the error, we first set the domain for averaging as a 20 minute-wide moving window, with a step size of 10 s. Since frequency-time spectrograms of wavevectors and background magnetic fields are roughly constant in time within each window (Figures 1 and 3), we use temporally averaged wavevectors and magnetic fields to build a new coordinate for mode decomposition. Then, we average the decomposition results overall 20 minute-wide windows.

According to the definition of Elsasser spectra (Bruno & Carbone 2013), we calculate magnetic energy $E_b = \frac{1}{2} \mathbf{b}^2$, kinetic energy $E_v = \frac{1}{2} \mathbf{v}^2$, and total energy $E_t = E_b + E_v$. As described in Section 2, the time series of velocity perturbation is transformed by FFT with three-point smoothing. Combined with the SVD method, the velocity perturbation (\mathbf{v}_k) as a function of wavevectors is projected onto the corresponding

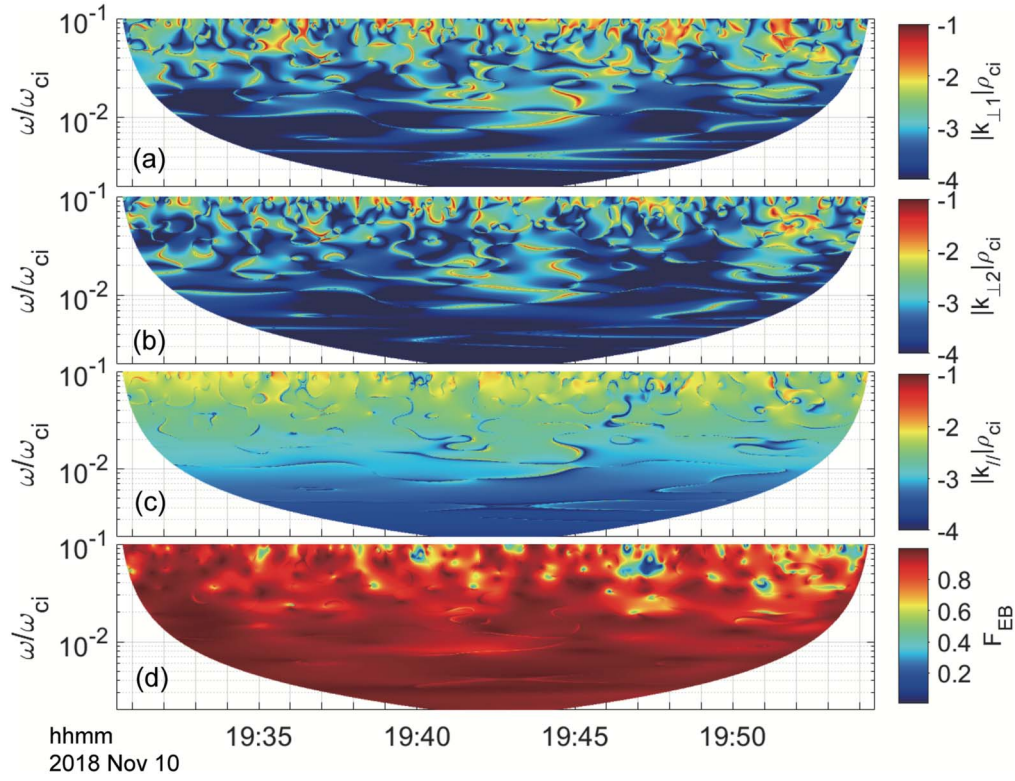


Figure 3. (a)–(c) The spacecraft-frame frequency-time spectrograms of wavevectors \mathbf{k} in the field-aligned coordinates. (d) electromagnetic planarity F_{EB} .

displacement vectors ξ ($\xi_{\text{Alfvén}}$, ξ_{fast} , and ξ_{slow} , see Figure 2(a)). Then the magnetic field perturbation and density are calculated based on the ideal MHD theory.

Figure 4(a) shows the comparison between the sum of the magnetic power of three MHD modes calculated based on the ideal MHD theory (purple; $P_{b,3\text{modes}} = P_{b,\text{Alfvén}} + P_{b,\text{fast}} + P_{b,\text{slow}}$) and the magnetic power directly obtained by FFT on magnetic field data (black; $P_{b,\text{obs}} = P_{b,R} + P_{b,T} + P_{b,N}$) in the spacecraft frame, where the error bars denote the standard deviation. $P_{b,3\text{modes}}$ and $P_{b,\text{obs}}$ are in good agreement when the frequency f_{sc} is less than ~ 0.026 Hz (marked by the red vertical dashed line in Figure 4(a)), confirming the validity of our mode decomposition procedure. The MHD frequency range can be considered as $f_{sc} \sim [0.004, 0.026]$ Hz.

The energy fraction of different modes at the MHD scale is estimated by

$$P_{\text{MEM}} = 100\% \times \frac{\sum_k |U_{k,m}(\mathbf{b})|^2}{\sum_{k,m} (|U_{k,m}(\mathbf{b})|^2 + |U_{k,m}(\mathbf{v})|^2)}, \quad (7)$$

$$P_{\text{KEM}} = 100\% \times \frac{\sum_k |U_{k,m}(\mathbf{v})|^2}{\sum_{k,m} (|U_{k,m}(\mathbf{b})|^2 + |U_{k,m}(\mathbf{v})|^2)}. \quad (8)$$

Here, P_{MEM} and P_{KEM} represent magnetic and kinetic energy fractions, respectively. The spectra $U_{k,m}(\mathbf{v})$ are the energy density for each mode, calculated by the velocity perturbation (\mathbf{v}_k) along the corresponding displacement vectors at each wavevector scale. The spectra $U_{k,m}(\mathbf{b})$ are calculated based on Equation (2), where \mathbf{b} is normalized by $\sqrt{\mu_0 \rho_0}$ (Bruno & Carbone 2013). For Alfvén and fast modes, the kinetic energy fraction is roughly equal to the magnetic fraction, where $P_{\text{MEA}} \sim P_{\text{KEA}} \sim 31\%$, $P_{\text{KEf}} \sim 17\%$, and $P_{\text{MEf}} \sim 16\%$. For slow

modes, the kinetic energy fraction P_{KEs} accounts for $\sim 5\%$, whereas their magnetic energy fraction P_{MEs} is negligible.

Figures 4(b)–(e) show the power spectral densities (PSDs) of each MHD mode in the spacecraft frame, where red, green, and blue curves represent Alfvén, fast, and slow modes, respectively. In Figure 4(b), total power is dominated by Alfvén modes, in agreement with the significantly Alfvénic features shown in Figures 1(f)–(h). Fast modes make a considerable contribution to total power, even comparable to Alfvén modes as the frequency increases. Slow modes play a limited part in total power. In Figure 4(c), similar proportions are shown in kinetic power. The slow-mode kinetic power is smaller than those of Alfvén and fast-mode modes but still holds a certain proportion (Figure 4(c)).

Figure 4(d) shows that magnetic power is almost provided by Alfvén and fast modes, whereas slow-mode contributions can be negligible. Figure 5 compares magnetic power spectra from direct observations with mode decomposition results (from Alfvén and fast modes) at the MHD scale. Magnetic field data are transformed into field-aligned coordinates (the same as Figure 3). The PSDs of $b_{\perp 1}$ and $b_{\perp 2}$ components of the magnetic field perturbation are much larger than those of b_{\parallel} component, indicating that magnetic field perturbations are mostly contained perpendicular to \mathbf{B}_0 . Moreover, $P_{b_{\perp 2}}$ with the scaling ~ -1.49 is comparable to Alfvén-mode magnetic power. $P_{b_{\perp 1}}$ and $P_{b_{\parallel}}$ are comparable to the perpendicular and parallel components of fast-mode magnetic power, respectively. Since the angle between \mathbf{V}_0 and \mathbf{k} is $\sim 2^\circ$ and \mathbf{V}_0 is almost in the $k\mathbf{B}_0$ plane in this event (sketched in Figure 2(a)), the $\mathbf{V}_0\mathbf{B}_0$ plane and $k\mathbf{B}_0$ plane are roughly coplanar. The Alfvén-mode magnetic field perturbations are perpendicular to the $k\mathbf{B}_0$ plane, leading to their magnetic power mainly along the $\mathbf{e}_{\perp 2}$ direction. Similarly, fast-mode magnetic field perturbations

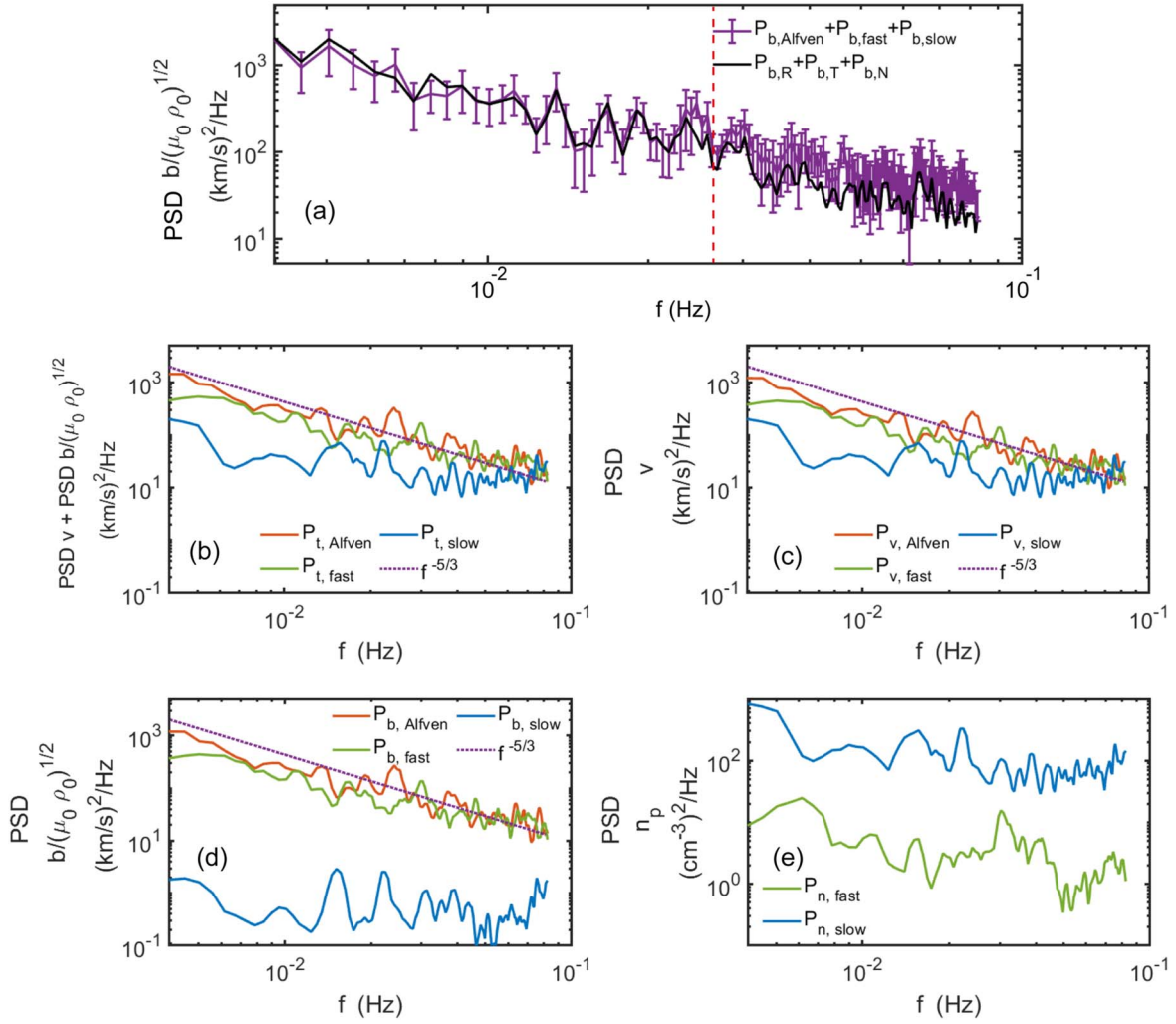


Figure 4. Power spectral densities from three MHD modes in the spacecraft frame during 19:30:30–20:14:30 UT. (a) the sum of magnetic power: the observed magnetic power (black; $P_{b,obs} = P_{b,R} + P_{b,T} + P_{b,N}$) and the magnetic power calculated based on the ideal MHD theory (purple; $P_{b,3modes} = P_{b,Alfvén} + P_{b,fast} + P_{b,slow}$). The red vertical dashed line represents the frequency $f_{sc} \sim 0.026$ Hz. The error bars stand for the standard deviation. (b) total power spectra; (c) kinetic power spectra; (d) magnetic power spectra; (e) proton density power spectra. Red, green, and blue curves represent Alfvén, fast, and slow modes, respectively. The purple dashed lines in (b)–(d) mark the Kolmogorov-like power law ($f_{sc}^{-5/3}$) as a reference.

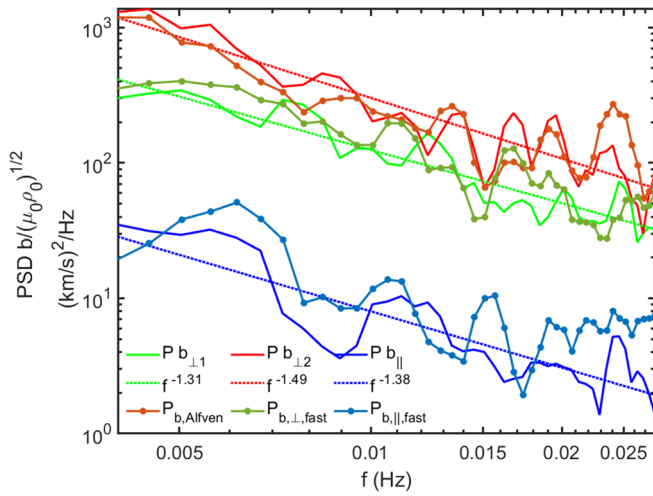


Figure 5. Results of the comparisons of magnetic power spectra from direct observations and mode decomposition from 19:30:30–20:14:30 UT.

are in the kB_0 plane, which explains the consistency between $P_{b, \perp}$ and $P_{b, \perp, fast}$.

Since slow-mode magnetic power is negligible and slow-mode density power is much larger than that of fast modes (Figure 4(e)), we speculate that fast modes dominate magnetic compressibility, and slow modes dominate density compressibility.

We compare PSDs of the compressible component from the direct observations with the decomposition results to verify our speculation on magnetic and density compressibility. In Figure 6(b), the parallel component of magnetic power ($P_{b, \parallel, obs}$) is obtained by FFT on magnetic field data from MAG, and fast-mode parallel magnetic power ($P_{b, \parallel, fast}$) is calculated based on the ideal MHD theory. $P_{b, \parallel, obs}$ is comparable to $P_{b, \parallel, fast}$ in the MHD regime, indicating that the parallel component of the magnetic field perturbation (δB_{\parallel}) is mainly provided by fast modes. The earlier assumption of $\delta |B| \approx \delta B_{\parallel}$ from slow modes is invalid in the radial-field solar wind. Moreover, Figure 6(c) shows the comparison of

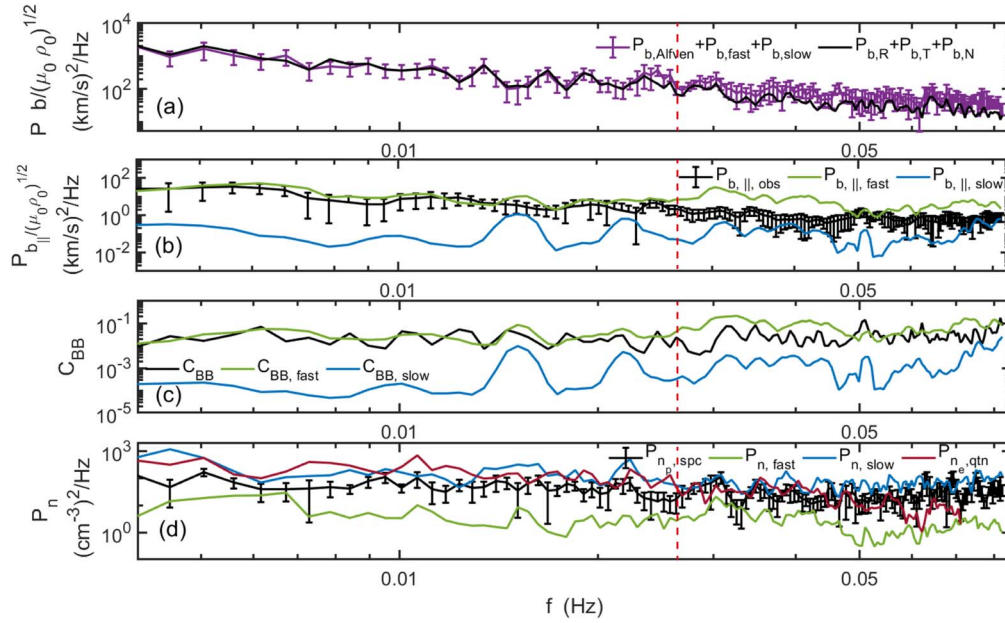


Figure 6. Comparison of compressible components of different modes during 19:30:30–20:14:30 UT in the spacecraft frame. (a) The sum of magnetic power in Alfvén units: the observed magnetic power (black; $P_{b,obs} = P_{b,R} + P_{b,T} + P_{b,N}$) and the magnetic power calculated based on the ideal MHD theory (purple; $P_{b,3modes} = P_{b,Alfvén} + P_{b,fast} + P_{b,slow}$). (b) Spectra of parallel component of magnetic power in units of Alfvén speed. (c) Spectra of magnetic compressibility $C_{BB} = \left(\frac{\delta |B|}{|B|}\right)^2$, $C_{BB,fast} = \frac{P_{b,||,fast}}{P_{b,3modes}}$, and $C_{BB,slow} = \frac{P_{b,||,slow}}{P_{b,3modes}}$. (d) Density power spectra: proton density power $P_{n,spc}$ from SPC, electron density power $P_{n,qtn}$ from QTN, and density power provided by fast modes $P_{n,fast}$ and slow modes $P_{n,slow}$. The error bars represent the standard deviation. The red vertical dashed line represents $f_{sc} \sim 0.026$ Hz.

magnetic compressibility. Fast-mode (slow-mode) magnetic compressibility is defined as the ratio of fast-mode (slow-mode) parallel magnetic power to total magnetic power: $C_{BB,fast} = \frac{P_{b,||,fast}}{P_{b,3modes}}$ ($C_{BB,slow} = \frac{P_{b,||,slow}}{P_{b,3modes}}$). The magnetic compressibility $C_{BB} = \left(\frac{\delta |B|}{|B|}\right)^2$ is comparable to $C_{BB,fast}$ and much larger than $C_{BB,slow}$, confirming that fast modes dominate magnetic compressibility.

In Figure 6(d), we compare PSDs of fluctuating density with those provided by fast and slow modes calculated based on the ideal MHD theory (black, proton density power $P_{n,spc}$ from SPC; red, electron density power $P_{n,qtn}$ from QTN; green, density power provided by fast modes $P_{n,fast}$; blue, density power provided by slow modes $P_{n,slow}$). Due to the relatively low time resolution of electron density data (~ 7 s), we obtain the PSD of electron fluctuating density by global FFT with three-point smoothing rather than the average moving windows used in proton data. Figure 6(d) shows that both $P_{n,spc}$ and $P_{n,qtn}$ are much larger than $P_{n,fast}$, indicating that fast modes cannot provide enough density perturbations. Therefore, it is likely that slow modes provide density perturbations from qualitative aspects. Moreover, $P_{n,slow}$ is systematically larger than $P_{n,spc}$, whereas at the same order of magnitude as $P_{n,qtn}$, further quantitatively verifying that density perturbations are mainly provided by slow modes. Given the consistency in magnetic power and electron density power, the systematic low $P_{n,spc}$ is likely caused by SPC data measurement errors (e.g., Liu et al. 2021). Therefore, the mode decomposition method used in this study provides an auxiliary for the calibration of density data.

3.3. Dispersion Relations and Collisionless Damping of Compressible Modes

Since the propagation time of wave packet is much less than nonlinear interaction time ($\frac{l}{V_A} \ll \frac{l}{v}$, where l is the characteristic length scale) and $k_{||} \gg k_{\perp} \sim 0$, perturbations exhibit more wave-like characteristics than turbulence. To investigate the propagations of MHD modes, we analyze their dispersion relations. First, according to the Doppler shift, the observed frequency in the plasma flow frame can be obtained by $\omega_{pf} = \omega_{sc} - \langle \mathbf{k} \rangle \cdot \langle \mathbf{V}_p \rangle$, where $\omega_{sc} = 2\pi f_{sc}$ is the observed frequency in the spacecraft frame, and $\langle \rangle$ represents the time average. The observed frequency ω_{pf} corresponds to the dominant frequency of perturbations at each wavevector scale. Second, based on ideal MHD theory, the wave phase velocity is given by

$$V_{ph,Alfvén} = V_A \cos \theta_{kB_0}, \quad (9)$$

$$V_{ph,\pm}^2 = \frac{1}{2} \{ (a^2 + V_A^2) \pm [(a^2 + V_A^2)^2 - 4a^2 V_A^2 \cos^2 \theta_{kB_0}]^{\frac{1}{2}} \}. \quad (10)$$

Here, “+” and “−” stand for fast and slow modes, respectively (Hollweg 1975). The theoretical frequency is calculated by $\omega_m = k V_{ph,m}$, where the subscript m represents Alfvén, fast, and slow modes.

Figure 7(a) displays the comparisons between the observed dispersion relation (black) and theoretical ones for Alfvén (red), fast (green), and slow (blue) modes in the plasma flow frame during 19:30:30–20:14:30 UT. The wavevectors and frequencies are normalized by average proton gyro-radius and gyrofrequency (ρ_{ci} and ω_{ci}), respectively. The dispersion

relations of Alfvén and fast modes are similar because of $k_{\parallel} \gg k_{\perp}$ and the low plasma β value. Both dispersion relations are in reasonable agreement with the observed results at $\frac{\omega}{\omega_{ci}} < 0.083$, demonstrating that Alfvén and fast modes dominate the MHD perturbations. The existence of the dominant dispersion relation across most of the spectrum further proves the validity of the SVD approach. Only when $\frac{\omega}{\omega_{ci}} > 0.083$, theoretical dispersion relations deviate from observations. The plasma-frame frequency $\frac{\omega}{\omega_{ci}} \sim 0.083$ corresponds to $f_{sc} \sim 0.026$ Hz in the spacecraft frame, consistent with the MHD frequency range identified by comparing magnetic power in Figure 4(a).

Figure 7(b) shows that the wave propagation angle is close to 180° , indicating the waves propagate roughly antiparallel to the background magnetic field. Due to average $\langle \theta_{kB_0} \rangle \sim 163^\circ$ at the MHD scale, Alfvén-mode phase velocity $V_{ph,Alfvén}$ is roughly equal to that of fast mode ($V_{ph,fast}$), explaining the similar dispersion relations between fast and Alfvén modes.

We investigate the possible effects of collisionless damping of each mode on solar wind heating in Figure 8. In contrast to weakly damped Alfvén modes, compressible modes undergo an intense collisionless wave-damping process, contributing to solar wind heating. The damping rate of fast modes of frequency ω for $\beta \ll 1$ and $\theta_{kB_0} \sim 1$ (Ginzburg 1961; Yan & Lazarian 2004; Petrosian et al. 2006) is given by

$$\gamma_{fast} = \omega \frac{\sqrt{\pi\beta}}{4} \frac{\sin^2 \theta_{kB_0}}{\cos \theta_{kB_0}} \left[\sqrt{\frac{m_e}{m_p}} \exp \times \left(\left(-\frac{m_e}{m_p \beta \cos^2 \theta_{kB_0}} \right) + 5 \exp \left(-\frac{1}{\beta \cos^2 \theta_{kB_0}} \right) \right) \right]. \quad (11)$$

The kinetic damping rate of slow modes (Galeev & Sudan 1983) is given by

$$\gamma_{slow} = \frac{|k| a}{2 |\cos \theta_{kB_0}|} \left(\frac{1}{8} \pi \frac{m_e}{m_p} \right)^{\frac{1}{2}} \left(1 - \frac{\cos 2\theta_{kB_0} \left[\left(\frac{a^2}{V_A^2} \right) \cos 2\theta_{kB_0} - 1 \right]}{\left[1 + \frac{a^4}{V_A^4} - 2 \left(\frac{a^2}{V_A^2} \right) \cos 2\theta_{kB_0} \right]^{\frac{1}{2}}} \right). \quad (12)$$

Here, m_e and m_p are the electron and proton mass, respectively.

Figure 8(a) shows the comparison of the damping rates of compressible modes. For each mode, the damping rate increases with increasing frequency. At the MHD scale, γ_{slow} (blue) is systematically larger than γ_{fast} (green), suggesting that slow modes suffer more intense collisionless damping. Moreover, fast-mode damping is affected by the wave propagation angle θ_{kB_0} . γ_{fast} enlarges when θ_{kB_0} approaches 90° (Yan & Lazarian 2004), likely because more plasmas can be trapped and interact with fast-mode waves at more significant magnetic compression. In contrast, γ_{slow} is scarcely influenced by θ_{kB_0} under the condition of quasi-antiparallel propagation.

Figure 8(b) shows wave energy damping power for fast and slow modes, which is defined as the product of the damping rate (γ) and the mean energy density of the wave (U), where $U_{fast} = \frac{1}{2} v_{fast}^2$ and $U_{slow} = \frac{1}{2} v_{slow}^2$. The fast-mode energy damping power $\gamma_{fast} U_{fast}$ accounts for $14.6\% \pm 3.9\%$ of fast-mode kinetic power ($P_{v,fast}$) in a 95% confidence interval at the MHD

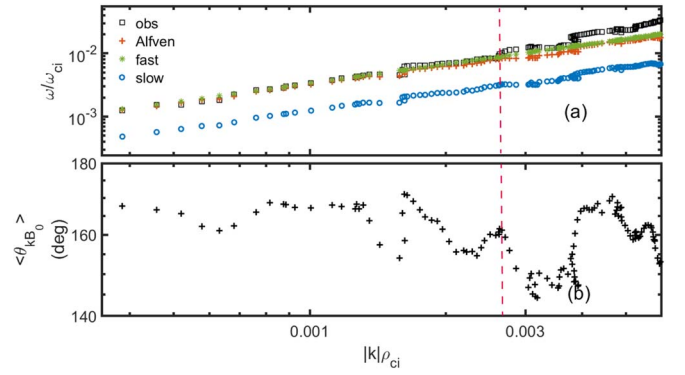


Figure 7. (a) Dispersion relations in the plasma flow frame during 19:30:30–20:14:30 UT. (b) The interval-averaged wave propagation angle. The wavevectors and frequencies are normalized by average proton gyro-radius and gyrofrequency (ρ_{ci} and ω_{ci}), respectively. The red vertical dashed line corresponds to $\frac{\omega}{\omega_{ci}} \sim 0.083$.

scale. Moreover, the slow-mode energy damping power $\gamma_{slow} U_{slow}$ accounts for $32.2\% \pm 4.0\%$ of slow-mode kinetic power ($P_{v,slow}$). Since $P_{v,fast}$ is much larger than $P_{v,slow}$ (Figure 4(c)), $\gamma_{fast} U_{fast}$ is roughly comparable to $\gamma_{slow} U_{slow}$. In this process, wave energy can be converted into plasma energy by collisionless damping of compressible modes.

To further quantitatively explore their possible contributions to solar wind heating, we calculate the fast-mode energy damping rate by $\epsilon_{fast} = \int \gamma_{fast} U_{fast} df$ and slow-mode energy damping rate by $\epsilon_{slow} = \int \gamma_{slow} U_{slow} df$ at the MHD scale. Results show $\epsilon_{fast} \sim 2.66 \times 10^5 \text{ J kg}^{-1} \text{ s}^{-1}$ and $\epsilon_{slow} \sim 2.74 \times 10^5 \text{ J kg}^{-1} \text{ s}^{-1}$, roughly consistent with the heating rate ($\sim 2 \times 10^5 \text{ J kg}^{-1} \text{ s}^{-1}$ at the first PSP perihelion) estimated by the global heliospheric simulations (Bandyopadhyay et al. 2020).

Figure 8(c) shows that slow-mode kinetic PSD (blue; $P_{v,slow}$) is closely related to the proton thermal kinetic PSD (pink; $P_{v,thermal}$), with a correlation coefficient of ~ 0.80 . The proton thermal kinetic energy is defined as $\frac{1}{2} w_p^2$, where $w_p = W_p - \langle W_p \rangle$ are thermal velocity perturbation of the protons. According to mode decomposition analysis and the continuity equation, slow-mode velocity perturbation (along ξ_{slow} in Figure 2(a)) mainly aligns with the background magnetic field and provides most density perturbations. Therefore, we deduce that slow modes may modulate the motion of protons, resulting in thermal energy variations and the inhomogeneous temperature of the plasma.

4. Discussion

During the first PSP encounter, we identified 15 events (see Table 1) based on the selection criteria described in Section 2.2. All the events show similar properties to the representative case presented above, such as a high degree of Alfvénicity, stable wavevectors, low magnetic compressibility mainly provided by fast modes, and low density compressibility primarily resulting from slow modes. All our events propagate anti-sunward based on the directions of wavevectors. One possible explanation for the absence of sunward reflected waves is that we can only identify the stronger one when both sunward and anti-sunward waves exist simultaneously. The spacecraft is so close to the Sun that sunward waves do not have enough time to develop sufficiently, and anti-sunward waves dominate (14.6 times more energy in the anti-sunward waves than sunward waves

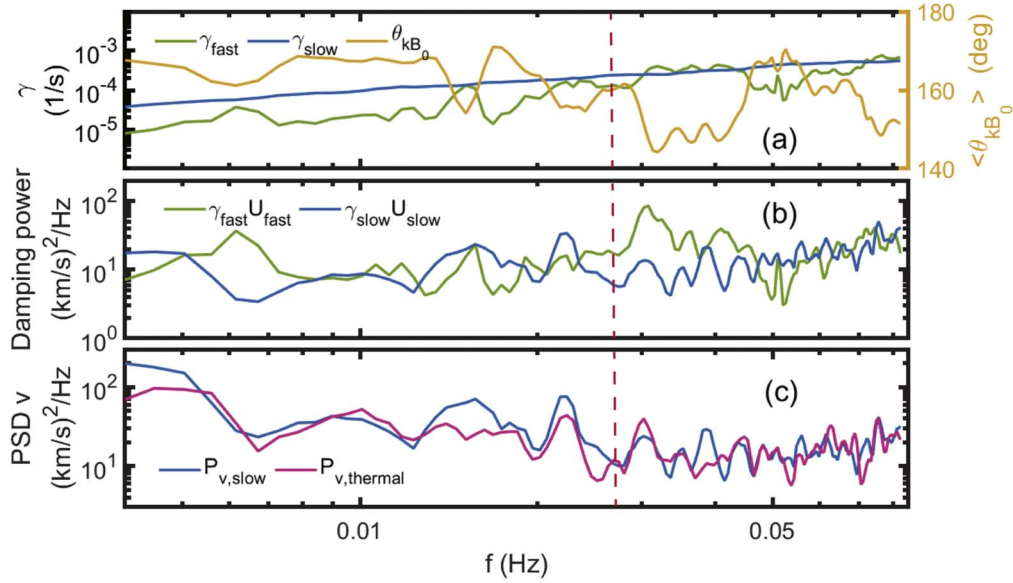


Figure 8. (a) Fast-mode damping rate γ_{fast} , slow-mode damping rate γ_{slow} , and the interval-averaged wave propagation angle. (b) Wave energy damping power. (c) Slow-mode kinetic power spectral density ($P_{v,\text{slow}}$) and the proton thermal fluctuating kinetic PSD (pink; $P_{v,\text{thermal}}$). The red vertical dashed line marks $f_{\text{sc}} \sim 0.026$ Hz.

Chen et al. 2019). The nonlinear interaction is weak, with waves dominating in one direction, and cannot generate strong turbulence.

Comparing with previous studies on MHD mode composition of solar wind turbulence (Chaston et al. 2020; Zhu et al. 2020), we set more stringent criteria to guarantee the validity of the single plane-wave assumption and combine the SVD and mode decomposition method (Cho & Lazarian 2003) to perform mode decomposition in wavevector space. In the quiet radial-field solar wind, the energy fraction of Alfvén mode is $\sim 45\%$ – 83% , roughly comparable to the results of Chaston et al. (2020) outside field reversals ($\sim 50\%$ – 60%). In contrast with them, slow modes ($\sim 1\%$ – 19%) occupy a much lower proportion than fast mode ($\sim 16\%$ – 43%) and could even be negligible in some events. The differences come from the sources of perturbations. Considering the limitation of the plane-wave assumption, we analyze the perturbations in the rigorous radial-field solar wind, wherein fast modes show more Alfvénic characteristics, and compressible modes occupy less proportion than those outside field reversals. The new mode decomposition method, apart from providing with energy fraction, makes it possible to quantitatively analyze the role of each MHD mode in kinetic, magnetic, and density power spectra. Thereby the contributions of each mode to magnetic and density compressibility are quantified. Moreover, we determine the collisionless damping of each mode, revealing the role of compressible modes in solar wind heating. These results will help us further understand the nature of solar wind turbulence at the MHD scale.

The MHD perturbations in the radial-field solar wind typically have a small θ_{kB_0} (approaching $0^\circ/180^\circ$). Figure 2(a) shows a schematic illustration of the vectors in the decomposition coordinate at $\theta_{kB_0} \sim 160^\circ$, where the angle between \mathbf{V}_0 and \mathbf{k} is around 2° , and \mathbf{V}_0 is almost in the kB_0 plane. $\hat{\mathbf{k}}_\perp (\perp \mathbf{B}_0)$, $\hat{\mathbf{k}}_\parallel (\parallel \mathbf{B}_0)$, and $\hat{\mathbf{k}}_\perp \times \hat{\mathbf{k}}_\parallel$ are unit vectors along the orientations of coordinate axes. As we can see, the fast-mode fluctuating velocities (along ξ_{fast}) are mainly perpendicular to \mathbf{B}_0 in the kB_0 plane, suggesting that their transverse components dominate. Transverse components of fast modes

propagating along \mathbf{B}_0 show similar characteristics to Alfvén modes, explaining the observed high-degree Alfvénicity. Besides, slow-mode fluctuating velocities (along ξ_{slow}) almost align with \mathbf{B}_0 in the kB_0 plane, indicating that slow modes are primarily acoustic.

Furthermore, the magnetic field perturbations are determined based on the linearized induction equation ($\omega \mathbf{b}_k = \mathbf{k} \times (\mathbf{B}_0 \times \mathbf{v}_k)$). The density perturbations are related to the angles between \mathbf{k} and \mathbf{v}_k , based on the continuity equation (Equation (3)). Thus, it is easy to understand that fast modes provide most of the parallel components of the magnetic field perturbations but only tiny density power. By contrast, slow modes dominate density power whereas only provide a tiny amount of magnetic power. Therefore, both in fast-mode and slow-mode perturbations, the apparent correlation of n and \mathbf{b} cannot be observed in the radial-field solar wind.

Only when θ_{kB_0} is approaching 90° , can fast modes produce significant density perturbations based on Equations (3) and (6), and slow modes can produce significant magnetic field perturbations based on Equations (2) and (5). Owing to the enhancements of fast-mode damping rate with θ_{kB_0} (e.g., Yan & Lazarian 2004), it is difficult to identify fast modes based on the positive correlation of n and \mathbf{b} . By contrast, highly oblique slow waves are less damped and exist in the form of non-propagating PBSs (e.g., Verscharen et al. 2019). These findings illustrate why few fast waves are observed, whereas slow waves can be frequently detected based on the anticorrelated density-magnetic field strength (e.g., Yao et al. 2013; Shi et al. 2015; Zhao et al. 2019).

All radial-field solar wind events in this study show that fast modes provide most of the parallel components of magnetic power, dominating magnetic compressibility. As the Sun rotates, the flow in the inner heliosphere is still radial and not along the jetline, whereas the magnetic field creates a Parker spiral (Parker 1957), as sketched in Figure 2(b). The angle between the radial direction and the Parker spiral direction increases with the heliocentric distance thereby. Since the angle between \mathbf{V}_0 and \mathbf{k} is small in the radial-field solar wind (e.g., $\theta_{kV_0} \sim 2^\circ$ in the presented event), it is reasonable to assume that

waves propagate in the flow direction, implying that θ_{kB_0} enlarges with the heliocentric distance. Based on Equations (2) and (6), fast modes become increasingly compressive with the enlargement of θ_{kB_0} . Thus, we deduce that C_{BB} enhancements with the increasing heliocentric distance are attributed to more enhanced compressive fast modes, and the effects of fast modes on compressibility cannot be neglected.

In the radial-field solar wind, wave energy damping power accounts for a considerable proportion in wave kinetic power, such as $14.6\% \pm 3.9\%$ for fast modes and $32.2\% \pm 4.0\%$ for slow modes in the presented event. Wave energy can be released into plasma energy by collisionless damping of compressible modes. As θ_{kB_0} increases, fast modes suffer more intense damping, whereas slow modes with highly oblique propagation are less subject to weak collisionless damping (e.g., Yan & Lazarian 2004; Verscharen et al. 2019). Therefore, we speculate that fast modes may play a more critical role in plasma heating with increasing heliocentric distance. The radial evolution of each mode's contributions to compressibility and solar wind heating is beyond the scope of this paper. They will be the subjects of our future studies.

We acknowledge the limitations of the SVD method in combination with the mode decomposition study. The SVD provides a linear mapping relationship between frequency and wavevector, whereas \mathbf{v}_k represents the total velocity perturbations at each wavevector scale. Mode decomposition is performed in the space of wavevector, which is retrieved by SVD method and is the only available one currently from single-spacecraft measurement. We assume that \mathbf{v}_k transformed by the SVD method includes all perturbations from the three MHD modes at each wavevector. There is no physical reason for the wavevectors of all three modes to be the same. Nonetheless, this assumption hardly affects the results of mode decomposition of turbulence in the radial-field solar wind. We take event #15 as an example without loss of generality. The decomposition results show that the fraction of Alfvén modes ($\sim 62\%$) is slightly higher than that of fast modes ($\sim 33\%$), indicating that both Alfvén and fast modes determine the wavevectors. Moreover, fast modes show similar dispersion relations to Alfvén modes (Figure 7) in the low- β limit, suggesting the mixture of Alfvén and fast modes affects the SVD results little. As for the slow modes, because they only occupy a minor fraction ($\sim 5\%$), SVD cannot determine their propagation direction. Nonetheless, in low- β limit, the fluctuating velocity along the magnetic field should be mainly provided by slow modes. Even with slow modes propagated in a different direction, our mode decomposition method provides the lower limit of the contribution of slow modes, and the order of the magnitude is not expected to be affected. Due to the inherent temporal and spatial ambiguities of single-spacecraft measurements, the combination method might not be ideal, but one of the best options available until now.

5. Summary

In this study, we report PSP observations of sub-Alfvénic MHD perturbations in low- β radial-field solar wind from 2018 October 31 to November 12. We calculate wavevectors using the SVD method (Santolík et al. 2003) and separate MHD perturbations into three eigenmodes (Alfvén, fast, and slow modes) using the mode decomposition method (Cho & Lazarian 2003). Thereby, our research quantitatively analyzes the kinetic, magnetic, and density power spectra of each MHD

mode and the possible contributions to magnetic and density compressibility. Moreover, we find that collisionless damping of compressible modes may significantly affect solar wind heating based on the correlation of the wave energy damping rate and the heating rate. The specifics of our findings are summarized below.

1. The radial-field solar wind turbulence has a high degree of Alfvénicity, with the energy fraction of Alfvén modes dominating ($\sim 45\% - 83\%$) over those of fast modes ($\sim 16\% - 43\%$) and slow modes ($\sim 1\% - 19\%$). For Alfvén and fast modes, the kinetic energy fraction is roughly equal to the magnetic energy fraction (e.g., $P_{MEA} \sim P_{KEA} \sim 31\%$, $P_{KEF} \sim P_{MEF} \sim 17\%$ for event #15). For slow modes, the kinetic energy fraction P_{KEs} accounts for $\sim 5\%$ (event #15), whereas their magnetic energy fraction P_{MEs} is negligible.
2. All our events show that fast modes provide most of the parallel components of the magnetic field, dominating magnetic compressibility. Slow modes provide most of the density perturbations, dominating density compressibility.
3. Slow modes modulate the motion of protons, leading to thermal energy variations and the inhomogeneous temperature of the plasma. The energy damping rate of compressible modes is comparable to the solar wind heating rate from the simulations.

We would like to thank the members of the FIELD/SWEAP teams and the PSP spacecraft team. We thank Chijie Xiao for stimulating discussions. We acknowledge the use of data from FIELDS/PSP (<http://research.ssl.berkeley.edu/data/psp/data/sci/fields/12/>), SWEAP/PSP (<http://sweap.cfa.harvard.edu/pub/data/sci/sweap/>), and SQTN (<https://cdpp-archive.cnes.fr/>). Data analysis was performed using the IRFU-MATLAB analysis package available at <https://github.com/irfu/irfu-matlab> and the SPADAS analysis software available at <http://themis.ssl.berkeley.edu>.

ORCID iDs

S. Q. Zhao  <https://orcid.org/0000-0003-4268-7763>
 Huirong Yan  <https://orcid.org/0000-0003-2560-8066>
 Terry Z. Liu  <https://orcid.org/0000-0003-1778-4289>
 Mingzhe Liu  <https://orcid.org/0000-0003-2981-0544>
 Mijie Shi  <https://orcid.org/0000-0002-9201-5896>

References

- Andrés, N., Sahraoui, F., Hadid, L. Z., et al. 2021, *ApJ*, **919**, 19
 Bale, S. D., Badman, S. T., Bonnell, J. W., et al. 2019, *Natur*, **576**, 237
 Bale, S. D., Goetz, K., Harvey, P. R., et al. 2016, *SSRv*, **204**, 49
 Bandyopadhyay, R., Goldstein, M. L., Maruca, B. A., et al. 2020, *ApJS*, **246**, 48
 Barnes, A. 1967, *PhFI*, **10**, 2427
 Bavassano, B., Dobrowolny, M., Mariani, F., & Ness, N. F. 1982, *JGR*, **87**, 3617
 Bruno, R., & Carbone, V. 2013, *LRSP*, **10**, 2
 Chandran, B. D. G. 2005, *PhRvL*, **95**, 265004
 Chaston, C. C., Bonnell, J. W., Bale, S. D., et al. 2020, *ApJS*, **246**, 71
 Chen, C. H. K., Bale, S. D., Bonnell, J. W., et al. 2019, *ApJS*, **246**, 53
 Cho, J., & Lazarian, A. 2003, *MNRAS*, **345**, 325
 Cranmer, S. R., & van Ballegoijen, A. A. 2012, *ApJ*, **754**, 92
 Dobrowolny, M., Mangeney, A., & Veltri, P. L. 1980, in IAU Symp. 91, Solar and Interplanetary Dynamics, ed. M. Dryer & E. Tandberg-Hassen (Dordrecht: Springer), 143
 Federrath, C. 2018, *PhT*, **71**, 38
 Fox, N. J., Velli, M. C., Bale, S. D., et al. 2016, *SSRv*, **204**, 7

- Galeev, A. A., & Sudan, R. N. 1983, *Basic Plasma Physics*, Vol. 1 (Amsterdam: North Holland)
- Ginzburg, V. L. 1961, *Propagation of Electromagnetic Waves in Plasma* (New York: Gordon & Breach)
- Glassmeier, K., Motschmann, U., & Stein, R. 1995, *AnGeo*, **13**, 76
- Grinstead, A., Moore, J. C., & Jevrejeva, S. 2004, *NPGeo*, **11**, 561
- Hollweg, J. V. 1975, *RvGeo*, **13**, 263
- Howes, G. G., Bale, S. D., Klein, K. G., et al. 2012, *ApJL*, **753**, L19
- Kasper, J. C., Abiad, R., Austin, G., et al. 2016, *SSRv*, **204**, 131
- Kumar, N., Kumar, P., & Singh, S. 2006, *A&A*, **453**, 1067
- Liu, M., Issautier, K., Meyer-Vernet, N., et al. 2021, *A&A*, **650**, A14
- Makwana, K. D., & Yan, H. 2020, *PhRvX*, **10**, 031021
- Moncuquet, M., Meyer-Vernet, N., Issautier, K., et al. 2020, *ApJS*, **246**, 44
- Parker, E. N. 1957, *JGR*, **62**, 509
- Petrosian, V., Yan, H., & Lazarian, A. 2006, *ApJ*, **644**, 603
- Porter, L. J., Klimchuk, J. A., & Sturrock, P. A. 1994, *ApJ*, **435**, 482
- Santolík, O., Parrot, M., & Lefeuvre, F. 2003, *RaSc*, **38**, 1010
- Shi, M. J., Xiao, C. J., Li, Q. S., et al. 2015, *ApJ*, **815**, 122
- Spanier, F., & Schlickeiser, R. 2005, *A&A*, **436**, 9
- Suzuki, T. K., Yan, H., Lazarian, A., & Cassinelli, J. P. 2006, *ApJ*, **640**, 1005
- Verscharen, D., Klein, K. G., & Maruca, B. A. 2019, *LRSP*, **16**, 5
- Yan, H., & Lazarian, A. 2015, *Magnetic Fields in Diffuse Media*, Vol. 407 (Berlin: Springer), 253
- Yan, H., & Lazarian, A. 2004, *ApJ*, **614**, 757
- Yan, H., & Lazarian, A. 2008, *ApJ*, **673**, 942
- Yao, S., He, J. S., Tu, C. Y., Wang, L. H., & Marsch, E. 2013, *ApJ*, **774**, 59
- Zhao, S. Q., Xiao, C. J., Wang, X. G., et al. 2019, *JGRA*, **124**, 10200
- Zhu, X., He, J., Verscharen, D., Duan, D., & Bale, S. D. 2020, *ApJL*, **901**, L3
- Zhuravleva, I., Churazov, E., Schekochihin, A. A., et al. 2014, *Natur*, **515**, 85